Nano Research

ISSN 1998-0124 CN 11-5974/O4
https://doi.org/10.1007/s12274-023-6402-7

Research Article

Towards efficient strain engineering of 2D materials: A four-points bending approach for compressive strain

Hao Li[1] (✉), Félix Carrascoso[1], Ana Borrás[2], Gloria P. Moreno[2], Francisco J. Aparicio[2,3], Ángel Barranco[2] (✉), and Andrés Castellanos Gómez[1] (✉)

[1] *Campus de Cantoblanco, Instituto de Ciencia de Materiales de Madrid, C. Sor Juana Inés de la Cruz, 3, 28049 Madrid, Spain*
[2] *Nanotechnology on Surfaces and Plasma Lab, Instituto de Ciencia de Materiales de Sevilla (CSIC-Universidad de Sevilla). C/Americo Vespucio 49, E-41092 Seville, Spain*
[3] *Departamento de Física Aplicada I, Escuela Politécnica Superior, Universidad de Sevilla, c/ Virgen de África 7, E-41011 Seville, Spain*

Received: 20 July 2023 / **Revised:** 7 December 2023 / **Accepted:** 8 December 2023

ABSTRACT

Strain engineering, as a powerful strategy to tune the optical and electrical properties of two-dimensional (2D) materials by deforming their crystal lattice, has attracted significant interest in recent years. 2D materials can sustain ultra-high strains, even up to 10%, due to the lack of dangling bonds on their surface, making them ideal brittle solids. This remarkable mechanical resilience, together with a strong strain-tunable band structure, endows 2D materials with a broad optical and electrical response upon strain. However, strain engineering based on 2D materials is restricted by their nanoscale and strain quantification troubles. In this study, we have modified a homebuilt three-points bending apparatus to transform it into a four-points bending apparatus that allows for the application of both compressive and tensile strains on 2D materials. This approach allows for the efficient and reproducible construction of a strain system and minimizes the buckling effect caused by the van der Waals interaction by adamantane encapsulation strategy. Our results demonstrate the feasibility of introducing compressive strain on 2D materials and the potential for tuning their optical and physical properties through this approach.

KEYWORDS

uniaxial compressive strain, polymer encapsulation, differential reflectance spectroscopy, exciton tunability

1 Introduction

Strain engineering, as a powerful strategy to tune the optical and electrical properties of two-dimensional (2D) materials by deforming their crystal lattice, has appealed huge interest in the last years [1–4]. As compared with three-dimensional (3D) semiconductors, 2D materials could sustain ultrahigh strains, even up to 10%, due to the lack of dangling bonds on their surface that makes them almost ideal brittle solids [5, 6]. This remarkable mechanical resilience, together with a strong strain-tunable band structure of these family of materials, endows them a broad optical/electrical response upon strain. Generally, 2D materials could be strained in various ways, uniaxial/biaxial strain [7–16], homogenous/inhomogeous strain [17–23], etc. Based on above, related studies on strain engineering based on 2D materials are abundant and various straining systems are developed to meet different user needs. Among them multi-point systems are most commonly used ones, one can strain 2D nanoflakes by transferring it on a polymer substrate and then deflecting the loading points, which has provided an efficient strategy on studying the strain's effect on 2D materials [15, 24, 25].

Uniaxial tensile strain, as an external stimuli, has been investigated to introduce an excitonic shift in 2D materials, thus tuning the optical and physical properties [26, 27]. Opposite to tensile strain, compressive strain usually leads to a contrary tunability on the excitonic shift in 2D materials, which offers a giant possibility to tune the excitons and bandgap in a large range [28–30]. While related researches are really scarce due to a lack of an efficient straining system. For a regular three-points bending system, applying compressive strain is restricted by its mechanic structure, which results in a contact between flake and inner pivotal cylinder [15]. Theoretically two-points bending system offers a possibility to apply compressive strain on 2D materials while still remains barriers on the implementation with optical microscope since the sample position changes sizably along both vertical and horizontal axis during the straining process [25]. Apart from the mechanic issues, the van der Waals interaction in 2D materials is not tough enough to sustain the flakes under compression, leading to a slippage and delamination from substrate as a result of buckling [31]. Thus, constructing an efficient straining apparatus and developing a strategy to minimize buckling effect become a challenging issue which motivates our research interest.

Here, we have modified a homebuilt three-points bending apparatus, recently developed in our group [15, 32, 33], to transform it to a four-points bending apparatus that allows one to apply both compressive and tensile strain to samples while they are inspected under an optical microscope. The applied strain of

Address correspondence to Hao Li, lihao-zzu@outlook.com; Ángel Barranco, angel.barranco@csic.es; Andrés Castellanos Gómez, andres.castellanos@csic.es

the four-points bending apparatus is experimentally determined by measuring the distance between features in a sample with lithographic structures on its surface finding a good agreement with the strain calculated using a continuum mechanics model for elastic beams. We then test the operation of our straining apparatus using molybdenum disulfide (MoS_2) as test material. We apply both uniaxial compressive and tensile strain to single-, bi- and tri-layer (1L, 2L and 3L) MoS_2 with the assistance of this apparatus to study the effect of the strain on their reflectance spectra. We observed that the excitonic features, present in the spectra, red/blue shift under tensile/compressive strain. We found that single-layer MoS_2 flakes tend to slip/delaminate for moderate compressive strains of −0.31%, limiting substantially the range of strain-tunability of its optical properties. We show how a recently developed adamantane encapsulation can strengthen the adhesion of the flake on the substrate reflected by the enhancement of the gauge factor and maximum sustainable strain before slippage up to −1.25%. Further we study the statistical flake to flake variation of the compression gauge factor and maximum compression strain with 21 different MoS_2 flakes. Note that, there is still a lack of a facile and efficient straining strategy to proceed uniaxial compressive strain engineering study based on ultrathin 2D transition-metal dichalcogenide (TMD) materials. We thus aim to provide these details in this current work.

2 Experimental setup and calibration

2.1 Four-points bending setup

Figure 1 shows the construction of the homebuilt four-points bending setup. The construction of four-points bending straining setup is a modification of a three-points bending apparatus recently developed by our group. Briefly, the system is based on two identical Z manual micrometric lineal stages (MAZ-40-10. Optics Focus, see Fig. 1(a)). Homebuilt parts attached with two outer and two inner cylinders (MS1R/M, Thorlabs, see Figs. 1(b) and 1(c)) are then mounted on the stages, which will be used as the pivots of the four-points bending setup. Permanent magnets are glued on the corners under the pedestal thus the stage could be adhered to a magnetic steel base used to transport the setup. Generally, one can introduce both tensile and compressive strain easily by fixing the inner cylinders and deflecting the outer cylinders as shown in Figs. 1(d) and 1(e), respectively.

2.2 Strain calibration

Generally, in a bending setup-based strain engineering experiments the strain is calculated using continuum mechanics formulas which enable one to obtain the applied strain from experimental parameters like the distance between the pivotal points, the thickness of the substrate and its deflection. In the aspect of four-points bending setup where the loading span is 1/3 of the support span (as Fig. 2(a) shows), the calculated strain $\varepsilon_{(c)}$ could be given by [34, 35]

$$\varepsilon_{(c)} = \frac{27Dt}{5L^2} \quad (1)$$

In Eq. (1), D represents the deflection of the substrate, t means the thickness of the substrate, and L is the distance between two outer pivotal points. In order to investigate the accuracy of this continuum mechanics formula on our homebuilt four-points bending setup, we have measured experimentally the strain following a calibration method recently developed by our group. Basically, an array of photoresist pillars is fabricated on the surface of polycarbonate (PC) and mylar (polyester) substrate by photolithography method. Further we place the substrate on the bending setup and monitor the distance between the center points of the first and the final pillars (as Fig. 2(b) shows) under tension and compression by quantitative analysis of optical microscopy images with Gwyddion software, note that the laser is focused on the central photoresist pillars to ensure the accuracy of measured strain and eliminate the difference between measured strain and local strain. The measured strain $\varepsilon_{(m)}$ can be then extracted from the measurements as Eq. (2) presents

$$\varepsilon_{(m)} = \frac{l - l_0}{l_0} \quad (2)$$

where l_0 is the distance between pillars at zero deflection and l is the distance between pillars at a given deflection recorded by every 0.5 mm (a full round) from 0 mm (initial place). As Fig. 2(b) shows, the pillars distance clearly changes under a tensile/compressive strain of 1.04%/−1.04% (maximum deflection of 10 mm, 20 rounds), respectively. Further we have studied the relationship between the deflection and the measured strain for both PC and mylar substrates, from which a clear linear dependency could be observed (Fig. 2(c)). Also Fig. 2(d) represents the experimentally measured strain vs. the calculated strain. The dataset accurately follows a line with slope of 1, indicating an excellent correspondence between the actual applied

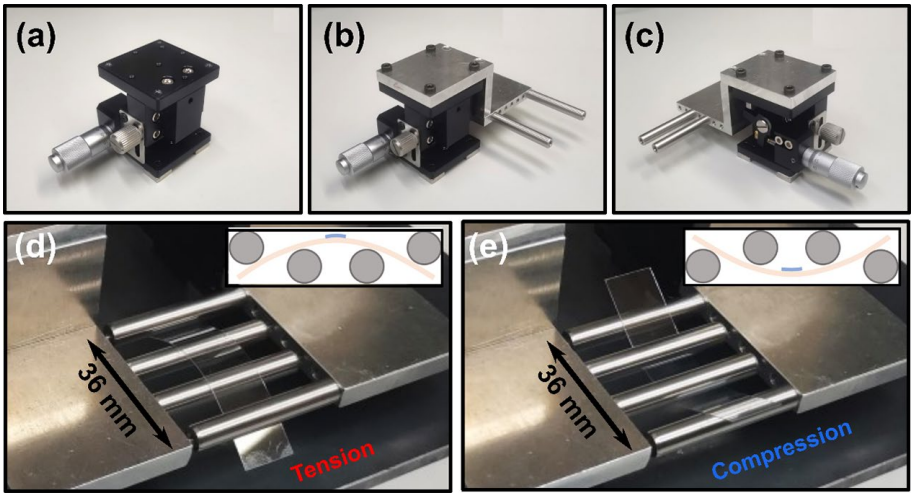

Figure 1 Homebuilt four-points bending setup for uniaxial tensile/compressive strain experiments on 2D materials. (a) Picture of one of the manual Z linear stages used for the assembly of the setup. (b) and (c) Pictures of the two manual Z stages after attaching the homemade parts with 2 outer cylinders and 2 inner cylinders, respectively. Pictures of the assembled setup with a flexible polycarbonate substrate under (d) tensile and (e) compressive strain test (insets show the cartoon illustrations of strained status under tension and compression, respectively).

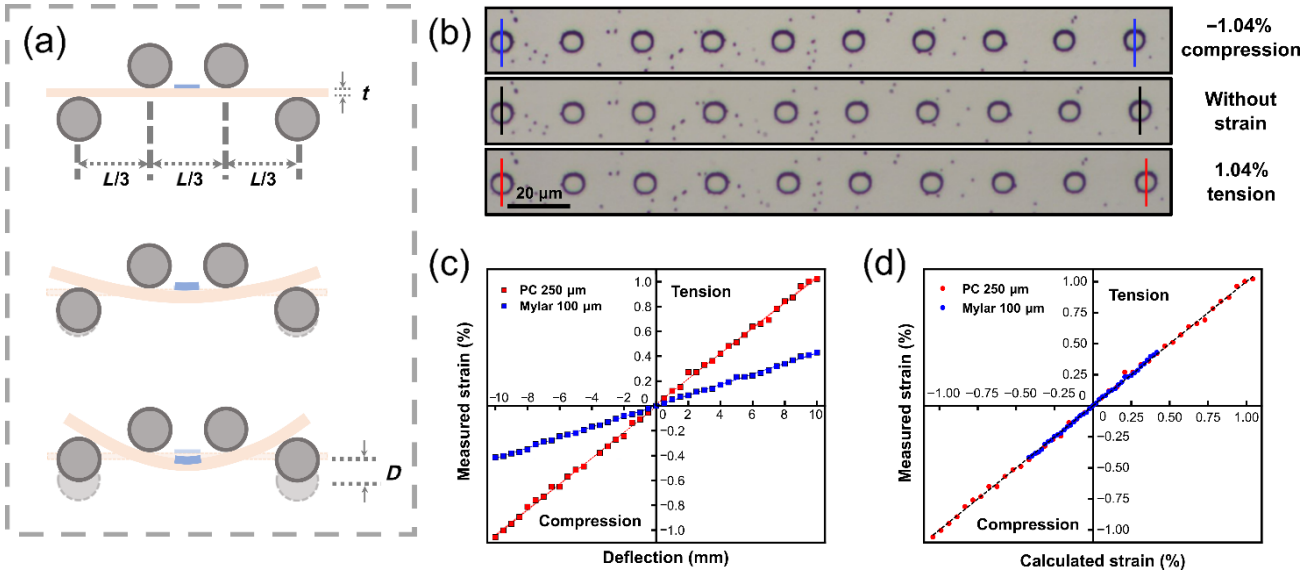

Figure 2 Calibration tests of the four-points bending setup. (a) Scheme of the four-points bending experiment indicating the relevant experimental magnitudes under compressive strain: distance between pivotal points (L), thickness of the substrate (t) and deflection of the substrate (D). (b) Optical microscopy images of photoresist micropillars patterned on the surface of a PC substrate with a thickness of 250 μm before and after applying tension and compression on the substrate, respectively. The strain applied on the substrate is experimentally measured by the displacement of the pillars. (c) Measured strain as a function of D for substrates with different thickness (PC and Mylar) and the fitted value (lines). (d) Relationship between the measured strain values and calculated strain using Eq. (1) for different substrates. A straight dashed line with slope = 1 is plotted to illustrate the small deviations with respect to the perfect agreement. Note: L is set as 36 mm for all these tests.

strain and the one calculated with the continuum mechanics formula. In principle, since the measured strain is supposed to be lower than the calculated strain due to nonuniform strain distribution, the excellent correspondence might benefit from a modest strain range and quantitative analysis on the central pillars.

3 Result and discussion

Figure 3(a) presents the reflectance spectra of exfoliated 1L MoS_2 under compressive strain from 0% to −0.42%, peaks A and B represent excitonic peaks at ~ 1.9 and ~ 2.0 eV, respectively, corresponding to the excitons generated by the direct bandgap transitions at K point of the Brillouin zone as reported [36–38]. The spectrum shows a blueshift under compression while terminates at a strain of −0.31%, at where the slippage might occur because of buckling. Relevant excitonic shift of peaks A and B vs. strain could be extracted and plotted as Fig. 3(b) presents, exhibiting gauge factors, which is identified as the excitonic shift as a function of strain, of −26.7 and −19.3 meV/% respectively. A statistic study of 5 1L MoS_2 (see Figs. S1–S4 in the Electronic Supplementary Material (ESM)) samples reveals a weak compatibility between 1L MoS_2 and compression which possibly results from a slippage/delamination of the flake on the polymer substrate. On the basis of this, it is worth noting that the actual strain introduced in MoS_2 flakes is much lower than the applied strain induced by bending polymer substrate due to a low strain transfer efficiency, thus the development of an effective way of enhancing the strain transfer efficiency becomes crucial.

In order to overcome the barrier of slippage/delamination, we develop a method of adamantane ($C_{10}H_{16}$) plasma polymer encapsulation on the nanoflakes to enhance the adhesion between the flake and the substrate. As a nanometric film with an extremely low roughness (root mean square (RMS) < 0.3 nm) and high transparency (bandgap 4.1 eV) [39], adamantane offers a giant possibility on enhancing the interaction between the flake and substrate, giving rise to an excitonic shift in a large range potentially. Figure 3(c) displays the differential reflectance spectrum of adamantane-encapsulated 1L MoS_2 sample under compression of 0% to −1.35%. Herein, in order to study the maximum sustainable strain of encapsulated 1L MoS_2 samples, higher strain over −1.04%/1.04% could be obtained by further moving inner cylinders towards the opposite direction when outer cylinders reach the maximum. Note that the differential reflectance spectrum after encapsulation is inverted which results from interlayer phenomena, interpreted by the involvement of an optical media with a different reflective index according to a Fresnel-law-based model [40]. Additionally, a blueshift of the excitons of MoS_2 after encapsulation could be observed, which might result from the pre-strain. During the encapsulation process, the temperature is slightly higher than the room temperature, which means the polymer layer might shrink after cooling down to room temperature and introduce a pre-compression on the flake, leading to a blueshift of the excitons. Comparing with unencapsulated 1L MoS_2, the reflectance spectrum of encapsulated 1L MoS_2 presents a clear blueshift under compression up to −1.25%. Similar enhancement can be reflected by the gauge factor plots in Fig. 3(d), which reach −49.2 and −46.0 meV/% for peaks A and B, respectively. Based on above, one can validate the adamantane encapsulation being a powerful strategy of reducing slippage and enhancing adhesion between the MoS_2 flake and PC substrate. As far as we know, there are several studies working on the polymer encapsulation to enhance the strain transfer between the flake and the substrate. For instance, Liu et al. reported a simple method of encapsulating the monolayer 2D material in the flexible polyvinyl alcohol (PVA) substrate through spin-coating approach, reaching a modulation rate of ~ 136 meV/% for MoS_2 [41]; Zhao et al. used formvar resins as a buffering layer between graphene and polydimethylsiloxane (PDMS) to achieve a maximum uniaxial tensile strain of 3.3% in graphene [42]. In this work, although we are not able to reach a shift rate as high as reported in Liu's work, the enhanced gauge factor still reaches ~ 2 times of that obtained from unencapsulated samples and the maximum sustainable strain on encapsulated samples increases to ~ 4 times of that on unencapsulated samples. Note that the adamantane-substrate adhesion is tough enough to prevent being separated from the substrate by physical methods (sonication, heating, etc.). On the basis of this, the strong adhesion of adamantane with high Young's modulus not only enhances the strain transfer, but also protects the flake from air environment,

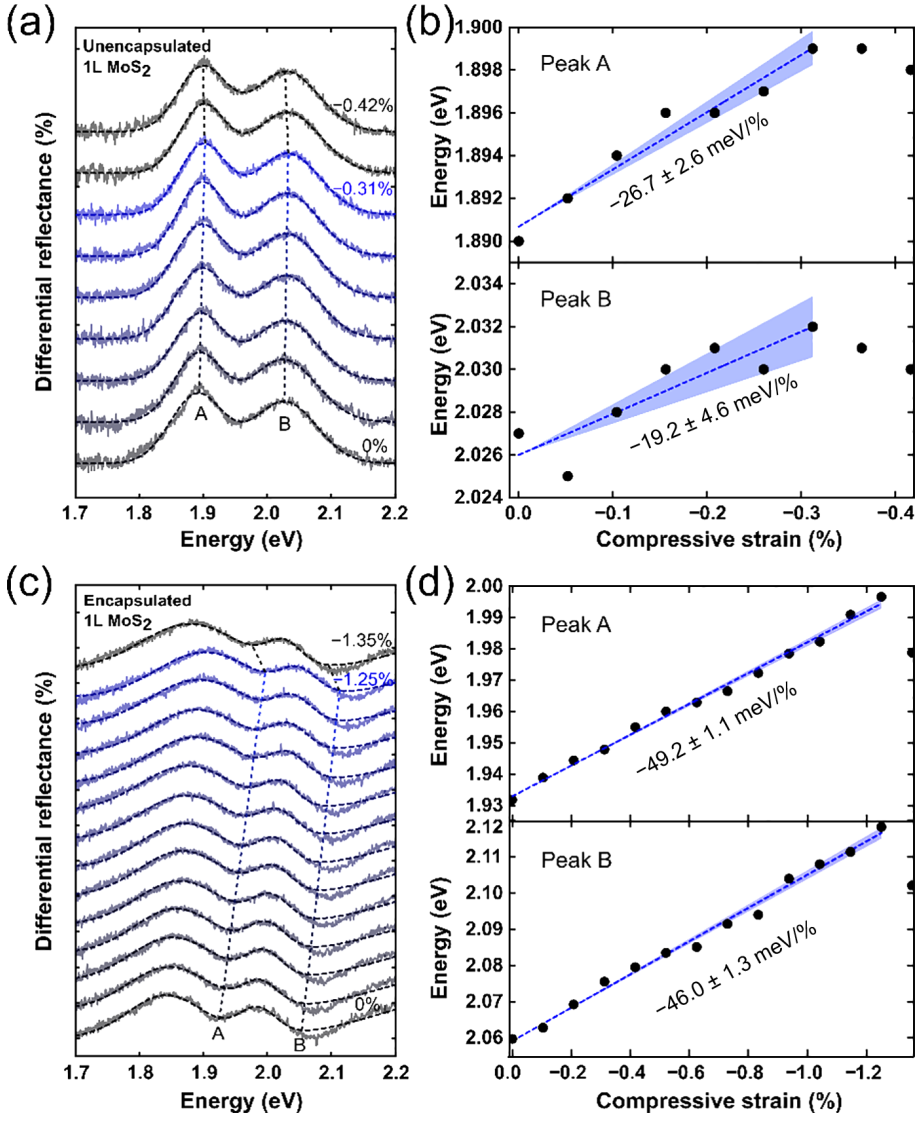

Figure 3 Differential reflectance spectroscopy test of unencapsulated and adamantane-encapsulated 1L MoS_2 samples under compressive strain. (a) Micro-reflectance spectra of 1L unencapsulated MoS_2 acquired under different compression level from 0% to −0.42%, slippage occurs at −0.31%, the fitting spectra are shown with dashed lines for each strain level. (b) A and B exciton energy values as a function of the applied uniaxial compressive strain on the basis of (a). (c) Micro-reflectance spectra of 1L encapsulated MoS_2 acquired under different compression level from 0% to −1.35%, slippage occurs at −1.25%, the fitting spectra are shown with dashed lines for each strain level. (d) A and B exciton energy values as a function of the applied uniaxial compressive strain on the basis of (c). A linear fit is employed to extract the gauge factor, which represents the spectral shift per % of uniaxial strain, is indicated in each panel (the shadowed area around indicates the uncertainty of the fitted value). Note that a smooth polynomial background has been subtracted from the spectra to facilitate identifying the exciton peaks. Further the spectra have been fitted to a sum of two Gaussian peaks to accurately determine the energy of the A and B excitonic features of unencapsulated samples, while for encapsulated samples, the spectra have been fitted to a sum of three Gaussian peaks to determine the energy of the A and B excitonic features at the valley (due to the effect of adamantane encapsulation).

which could be beneficial for those materials with high degradability, such as black phosphorus.

Further the availability of applying both tension and compression with this apparatus could be studied with the encapsulated 1L MoS_2. As Fig. 4(a) shows, the differential reflectance spectra of encapsulated 1L MoS_2 exhibit a clear redshift under a tensile strain from 0% to 1.04%. The corresponding A and B excitonic shift are plotted and fitted in Fig. 4(b), the redshift shows a linear trend with gauge factors of −74.0 and −43.2 meV/%, respectively. In the term of compressive strain, the differential reflectance spectra show a clear blueshift under a compressive strain from 0% to −0.88% (Fig. 4(d)), which could also be quantified from the corresponding A and B excitonic shift plotting with gauge factors of −51.6 and −60.3 meV/%, respectively (Fig. 4(c)), verifying that the compressive strain could tune the excitons of 1L MoS_2 in a compatible gradient as tensile strain. Nevertheless, a lower gauge factors obtained under compression compared with that obtained under tension is observed in our study. This might result from two aspects: Firstly, compression is, in principle, a source of structural instability in a two-dimensional material, as it can result in buckling or other types of out-of-plane deformations, which makes the flake easy to slip and reduce the strain transfer efficiency [43]; Also, contraction perpendicular to the strain direction is included using a typical value for the Poisson's ratio of the PC substrate. This means that when one applies compressive strain on the PC substrate, we assume a perpendicular tensile strain applied on the sample, further reduce the gauge factor under compressive strain as well [44]. Based on above, and thanks to the ability to apply both tensile and compressive strain one can easily tune the bandgap of 1L MoS_2 all the way from 1.870 to 1.985 eV with relatively moderate strain, which provides a huge potential in related strain-tunable electronic fields.

Identical strain-tunable differential reflectance tests have been

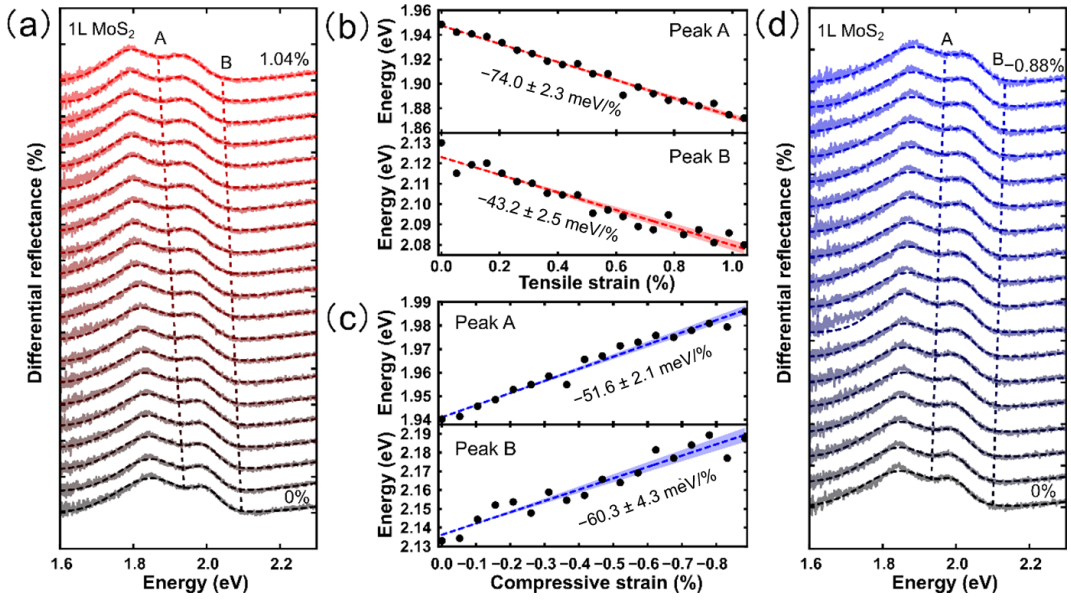

Figure 4 Strain-tunable differential reflectance tests on encapsulated 1L MoS_2 (Sample SE4) with four-points bending setup. Differential reflectance spectra acquired at different uniaxial (a) tensile (red) and (d) compressive (blue) strain levels, up to 1.04% and −0.88%, respectively. The fitting spectra are shown with dashed line for each strain level, (b) and (c) A and B exciton energy values as a function of the applied uniaxial (b) tensile (red) and (c) compressive (blue) strain. A linear fit is employed to extract the gauge factor, which represents the spectral shift per % of uniaxial strain, is indicated in each panel (the shadowed area around indicates the uncertainty of the fitted value).

carried out on 2L and 3L MoS_2 flakes before and after adamantane encapsulation. As the reflectance spectra show, for unencapsulated 2L and 3L MoS_2 flakes (see Figs. S5–S8 in the ESM), a shoulder peak appears between peaks A and B due to the interlayer interaction. Interestingly, we found that even for 2L and 3L unencapsulated samples (Figs. S5 and S7 in the ESM), the flakes could sustain a compressive strain up to −0.89% and −0.94%, respectively, while the gauge factors still remain a relatively-low value of −20.7 and −25.5 meV/% for peak A and even lower for peak B and interlayer peak. Regarding tensile strain, the 2L flake and 3L flake could sustain a tension of 1.04% (Figs. S6 and S8 in the ESM) and exhibit excitonic shift gauge factors of −25–−30 meV/% for all peaks. Meanwhile, the gauge factors of peak A obtained from adamantane-encapsulated 2L and 3L MoS_2 samples shown in Figs. S9 and S10 in the ESM could be up to −54.6 and −50.4 meV/% under compression up to −0.94%, on the aspect of tension test, the gauge factors of peak A are up to −52.1 and −54.6 mev/% for encapsulated 2L and 3L MoS_2 under a strain up to 1.04%, respectively. Based on above, the feasibility of the 4-points bending setup and adamantane encapsulation strategy could be validated on both single layer and multilayer flakes.

Further we study the flake-to-flake statistical variability of the strain tunability of the excitons by testing 21 MoS_2 samples under both tensile and compressive strain (including 7 unencapsulated samples in Figs. S1–S8 in the ESM and 14 encapsulated samples in Figs. S9–S21 in the ESM, the lateral size of all samples ranges from 20 to 50 μm). Figure 5(a) presents the gauge factor variation of 21 MoS_2 samples under compressive strain, both peaks A and B of encapsulated samples show gauge factors of approximately 2 times of that of unencapsulated samples, indicating a giant enhancement of adamantane encapsulation on the excitonic shift for both peaks A and B. Likewise an enhanced maximum sustainable compressive strain could be found in all encapsulated 1L MoS_2 samples (Fig. 5(b)). The adamantane encapsulation clearly offers 1L MoS_2 flake a much higher resistance to slippage/delamination. Detailed results of all 21 samples under both tensile and compressive strain are integrated as Table 1 summarizes. Note that the gauge factors of few encapsulated 1L samples are lower than other samples, which could due to unproper transfer, partially-efficient encapsulation, or wrinkled/damaged flake surface, leading to a lower strain transfer efficiency. Besides, interface quality and non-uniform strain distribution on the MoS_2 sheet have also been investigated to account for this variety since applied in-plane strain is able to effectively tune the friction of suspended nanoflakes in a reversible manner [45]. While in general, it is obvious to be observed that all the encapsulated samples (even SE7 with the lowest gauge factor) exhibit enhanced gauge factors than those unencapsulated ones, which reveals the efficiency of adamantane encapsulation strategy. In order to get an insight into the maximum strain that the 1L MoS_2 flake can suffer after encapsulation, several samples were subjected to uniaxial compressive strain until slippage occurs, revealing that a maximum sustainable strain of between −1.15% and −1.25% as shown in Fig. 3, and Figs. S22 and S23 in the ESM. Thus it can be seen that the maximum sustainable strain of the encapsulated flakes inevitably varies at a large strain level (−0.62% to −1.35%) due to the occurrence of interfacial slippage/buckling. On the basis of this, several strategies can be further developed to enhance the interfacial interaction, for instance, selection of large flakes with uniform and flat morphology, substrates with ultralow roughness, and encapsulating layer with a higher Young's modulus and stability. Apart from this, we have also carried out the reproducibility test by applying 5 compressive strain cycles from 0% to −1.04% then back to 0% with encapsulated 1L MoS_2 (see Fig. S24 in the ESM). The A and B excitonic shifts as a function of applied compressive strain are plotted in Figs. S25 and S26 in the ESM, presenting extremely consistent gauge factors on both strain loading/unloading processes, thus verifying an excellent reproducibility based on this four-points bending apparatus.

Based on above, one can conclude the distinctive advantages of four-points bending apparatus in comparison with other multi-points bending apparatus. Firstly, the flake could be positioned at almost same place during the whole test, which simplifies the light focusing compared with two-points bending apparatus on which the sample position varies along both vertical and horizontal axis under straining state; Secondly, the unique mechanic structure endows it a possibility to apply both tensile and compressive strain on 2D materials, which is not applicable with three-points bending apparatus; Lastly, the four-points bending apparatus also

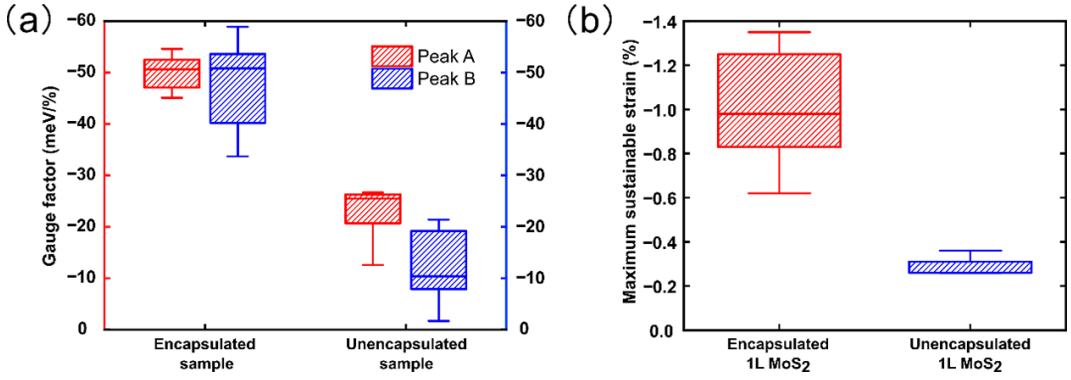

Figure 5 Statistical flake-to-flake variation in 21 different MoS_2 samples under compressive strain. (a) Box plot representation of the gauge factor values for peaks A and B of 14 encapsulated and 7 unencapsulated samples under uniaxial compression. (b) Box plot representation of maximum sustainable strain for 8 encapsulated and 5 unencapsulated 1L MoS_2 under compression.

Table 1 Summary of the exciton shift gauge factor and maximum sustainable strain upon uniaxial compression and tension for 21 different MoS_2 samples (strain only up to −1.04% and 1.04% for compression and tension, respectively). Note: S—single layer, B—bilayer, T—trilayer, E—encapsulated sample, and U—unencapsulated sample. The lateral size of all samples ranges from 20 to 50 μm

Sample		Gauge factor (meV/%, compression)		Maximum strain (compression)	Gauge factor (meV/%, tension)		Maximum strain (tension)
		Peak A	Peak B		Peak A	Peak B	
1L unencapsulated MoS_2	Sample SU1	−24.0 ± 3.2	−15.8 ± 8.5	−0.31%	—	—	—
	Sample SU2	−26.3 ± 8.1	−10.4 ± 4.8	−0.26%	—	—	—
	Sample SU3	−12.6 ± 2.4	−9.4 ± 2.9	−0.36%	—	—	—
	Sample SU4	−25.8 ± 9.0	−21.4 ± 3.1	−0.26%	—	—	—
	Sample SU5	−26.7 ± 2.6	−19.2 ± 4.6	−0.31%	—	—	—
1L encapsulated MoS_2	Sample SE1	−36.5 ± 2.0	−37.4 ± 1.4	−1.04%	−51.5 ± 2.2	−38.2 ± 2.4	1.04%
	Sample SE2	−47.1 ± 2.4	−35.4 ± 2.4	−0.83%	−58.4 ± 1.9	−37.9 ± 2.0	1.04%
	Sample SE3	−53.2 ± 2.5	−40.6 ± 2.0	−0.83%	−53.4 ± 2.3	−41.7 ± 1.6	1.04%
	Sample SE4	−51.6 ± 2.1	−60.3 ± 4.3	−0.88%	−74.0 ± 2.3	−43.2 ± 2.5	1.04%
	Sample SE5	−50.8 ± 5.0	−50.9 ± 18.4	−0.62%	−60.0 ± 2.0	−31.6 ± 1.7	1.04%
	Sample SE6	−49.4 ± 2.0	−51.5 ± 4.2	−0.98%	−57.4 ± 2.3	−31.1 ± 2.4	0.98%
	Sample SE7	−35.6 ± 3.3	−36.5 ± 4.8	−1.04%	−60.3 ± 1.4	−31.1 ± 2.1	0.98%
	Sample SE8	−49.6 ± 1.6	−40.2 ± 2.2	−0.67%	−61.0 ± 2.1	−26.3 ± 1.8	1.04%
		Peak A	Peak IL	Peak B	Peak A	Peak IL	Peak B	
2L unencapsulated MoS_2	Sample BU1	−20.7 ± 1.3	15.2 ± 2.2	7.9 ± 2.2	−0.89%	−29.2 ± 0.6	−30.5 ± 1.0	−24.7 ± 1.1	1.04%
	Sample BE1	−54.6 ± 2.0	—	−54.0 ± 1.3	−0.83%	−52.1 ± 1.0	—	−43.4 ± 0.7	1.04%
2L encapsulated MoS_2	Sample BE2	−53.6 ± 2.0	—	−52.3 ± 1.6	−0.88%	−53.1 ± 1.5	—	−44.2 ± 1.1	1.04%
	Sample BE3	−47.5 ± 1.7	—	−50.7 ± 1.3	−0.94%	−57.1 ± 1.5	—	−44.5 ± 1.4	1.04%
3L unencapsulated MoS_2	Sample TU1	−25.5 ± 1.3	−7.6 ± 1.9	1.7 ± 2.3	−0.94%	−27.6 ± 1.0	−25.0 ± 1.6	−27.8 ± 1.1	1.04%
	Sample TE1	−50.4 ± 1.8	—	−58.3 ± 1.9	−0.94%	−54.6 ± 1.5	—	−53.6 ± 1.5	1.04%
3L encapsulated MoS_2	Sample TE2	−52.5 ± 1.9	—	−51.3 ± 1.9	−0.94%	−48.8 ± 1.3	—	−47.5 ± 0.9	1.04%
	Sample TE3	−45.1 ± 2.3	—	−47.0 ± 1.7	−1.04%	−51.1 ± 1.8	—	−44.5 ± 2.0	1.04%

offers an potential to study the effect of uniaxial strain on 2D anisotropic materials by using a disk-like substrate and rotating the sample to apply strain along various crystalline orientations.

4 Conclusion

Herein, we constructed a homebuilt four-points bending apparatus and firstly reported a comprehensive experimental study of excitons shift in MoS_2 under compressive strain. The system was experimentally calibrated by directly measuring the distance between features on the surface of flexible substrates while strain was applied finding an excellent agreement with the strain calculated using continuum mechanics. We benchmarked this bending system by performing differential reflectance spectroscopy in single-, bi- and tri-layer MoS_2 under different strains. We found a clear blue/red shift under compressive/tensile strain. Interestingly, we found that pristine 1L MoS_2 tends to slip/delaminate at very moderate compressive strains and that adamantane encapsulation effectively helped to increase the adhesion improving both the maximum sustainable strain before slippage and the strain gauge factor of 1L, 2L, and 3L MoS_2. Finally, we performed a study of the statistical flake to flake variation by analyzing 21 different MoS_2 flakes.

5 Experimental section

5.1 Exfoliation of MoS_2 flakes

The bulk MoS_2 are obtained from molybdenite mineral (Molly Hill mine, Quebec, Canada). We adhere Nitto tape (Nitto SPV 224) to the bulk MoS_2 to peel off the bulk crystals, then we could obtain relatively-thinner bulk crystals by adhering another Nitto tape on the top of the first Nitto tape sample and repeating this process for few times. In order to obtain the final few-layered MoS_2 flakes we adhere a piece of Gel-Film (Gel-Pak, WF × 4 6.0 mil) on the Nitto tape sample and peel it off gently. Then we can identify 1L, 2L and 3L flakes because of their faint transmittance under an optical microscope operated in transmittance mode (Motic BA 310 MET-T optical microscope). Further accurate identification of the layers of MoS_2 flakes can be double-checked using differential reflectance spectroscopy [46].

5.2 Transfer of MoS_2 flakes on polymer substrate

Once the target MoS_2 flake is found, we use an all-dry deterministic placement method to transfer it on the center of the beam-like substrate [47]. Here we have utilized PC (thickness of 250 μm) and mylar (thickness of 100 μm) to proceed this research.

5.3 Adamantane encapsulation on the sample

A thin layer of adamantane plasma polymer was applied to the surface of a sample using a technique called remote plasma-assisted vacuum deposition (RPAVD) [48]. This method is beneficial for depositing layers of functional organic molecules that are sensitive and cannot be deposited through direct Ar plasma due to fragmentation. The adamantane powder (> 99% purity) used for the process was purchased from Sigma-Aldrich and was used as received. The deposition process involved the controlled sublimation of the powder in the downstream region of an Ar microwave electron cyclotron resonance (ECR) plasma. The deposition pressure was 10^{-2} mbar and the plasma power was 210 W. The temperature of the substrates was slightly above room temperature, as determined by a thermocouple connected to the sample holder. The sample holder was positioned about 10 cm from the plasma and oriented upside down to minimize plasma interaction with the surface. The evaporation rate was monitored with a calibrated quartz crystal monitor (QCM). A set of films were examined by spectroscopic ellipsometry to calibrate the QCM values and obtain reproducible thickness values. Reference films were also examined by spectroscopy ellipsometry to verify the thickness during each deposition process. The full details of the plasma source and reactor geometry can be found in related literatures [39, 49]. As a result of this process, an adamantane film with a thickness of approximately 50 nm was deposited on all samples in this research.

5.4 Strain-resolved differential reflectance spectroscopy

Once the sample is placed on the four-points bending apparatus, we mount the setup under the objective of the optical microscope which is integrated with a homebuilt micro-reflectance module based on a fiber-coupled CCD spectrometer (CCS200/M, Thorlabs) for collecting the spectra [41]. The flake is positioned at the center of two inner pivotal cylinders under microscope inspection, note that for four-points bending setup, each point on the area between the inner pivots should sustain equal strain [34]. Then the differential reflectance spectra are acquired under different strain levels. Here we use differential reflectance test instead of photoluminescence test to investigate the effect of strain on the exciton of MoS_2, for the propose of studying both A and B features, even interlayer feature for multilayers.

Acknowledgements

This work was funded by the European Research Council (ERC) under the European Union's Horizon 2020 research and innovation program (Nos. 755655, ERC-StG 2017 project 2D-TOPSENSE), the Ministry of Science and Innovation (Spain) through the project PID2020-115566RB-I00. We also acknowledge funding from the EU FLAG-ERA project To2Dox under the program PCI2019-111893-2. H. L. acknowledges the grant from China Scholarship Council (CSC) under No. 201907040070. Ana B. thanks the ERC Union's Horizon 2020 program (No. 851929 StG 2019 project 3DScavengers). We also thank the Spanish Ministry of Science and Innovation AEI/10.13039/501100011033 (No. PID2019-110430GB-C21), the EU ERDF (FEDER Operational Program (2014-2020), A way of making Europe) and the Consejería de Economía, Conocimiento, Empresas y Universidad de la Junta de Andalucía (Nos. P18-RT-3480, EMERGIA and US-1381057).

Funding note: Open Access funding provided thanks to the CRUE-CSIC agreement with Springer Nature.

Electronic Supplementary Material: Supplementary material (further details of all the MoS_2 samples, including unencapsulated and encapsulated samples, 1L/2L/3L MoS_2 samples, maximum sustainable strain test, reproducibility tests) is available in the online version of this article at https://doi.org/10.1007/s12274-023-6402-7.

References

[1] Naumis, G. G.; Barraza-Lopez, S.; Oliva-Leyva, M.; Terrones, H. Electronic and optical properties of strained graphene and other strained 2D materials: A review. *Rep. Prog. Phys.* **2017**, *80*, 096501.

[2] Jiang, H. J.; Zheng, L.; Liu, Z.; Wang, X. W. Two-dimensional materials: From mechanical properties to flexible mechanical sensors. *InfoMat* **2020**, *2*, 1077–1094.

[3] Bissett, M. A.; Tsuji, M.; Ago, H. Strain engineering the properties of graphene and other two-dimensional crystals. *Phys. Chem. Chem. Phys.* **2014**, *16*, 11124–11138.

[4] Chen, W. J.; Gui, X. C.; Yang, L. L.; Zhu, H.; Tang, Z. K. Wrinkling of two-dimensional materials: Methods, properties and applications. *Nanoscale Horiz.* **2019**, *4*, 291–320.

[5] Bertolazzi, S.; Brivio, J.; Kis, A. Stretching and breaking of ultrathin MoS_2. *ACS Nano* **2011**, *5*, 9703–9709.

[6] Li, W. B.; Qian, X. F.; Li, J. Phase transitions in 2D materials. *Nat. Rev. Mater.* **2021**, *6*, 829–846.

[7] Ahn, G. H.; Amani, M.; Rasool, H.; Lien, D. H.; Mastandrea, J. P.; Ager III, J. W.; Dubey, M.; Chrzan, D. C.; Minor, A. M.; Javey, A. Strain-engineered growth of two-dimensional materials. *Nat. Commun.* **2017**, *8*, 608.

[8] Liu, Z.; Amani, M.; Najmaei, S.; Xu, Q.; Zou, X. L.; Zhou, W.; Yu, T.; Qiu, C. Y.; Birdwell, A. G.; Crowne, F. J. et al. Strain and structure heterogeneity in MoS_2 atomic layers grown by chemical vapour deposition. *Nat. Commun.* **2014**, *5*, 5246.

[9] Duerloo, K. A. N.; Li, Y.; Reed, E. J. Structural phase transitions in two-dimensional Mo- and W-dichalcogenide monolayers. *Nat. Commun.* **2014**, *5*, 4214.

[10] Wang, S. W.; Medina, H.; Hong, K. B.; Wu, C. C.; Qu, Y. D.; Manikandan, A.; Su, T. Y.; Lee, P. T.; Huang, Z. Q.; Wang, Z. M. et al. Thermally strained band gap engineering of transition-metal dichalcogenide bilayers with enhanced light-matter interaction toward excellent photodetectors. *ACS Nano* **2017**, *11*, 8768–8776

[11] G.; Castellanos-Gomez, A.; Buscema, M.; Van Der Zant, H. S. J.; Steele, G. A.; Kuc, A.; Heine, T.; Schüller, C.; Korn, T. Control of biaxial strain in single-layer molybdenite using local thermal expansion of the substrate. *2D Mater.* **2015**, *2*, 015006

[12] Gant, P.; Huang, P.; De Lara, D. P.; Guo, D.; Frisenda, R.; Castellanos-Gomez, A. A strain tunable single-layer MoS_2 photodetector. *Mater. Today* **2019**, *27*, 8–13.

[13] Yang, R.; Lee, J.; Ghosh, S.; Tang, H.; Sankaran, R. M.; Zorman, C. A.; Feng, P. X. L. Tuning optical signatures of single- and few-layer MoS_2 by blown-bubble bulge straining up to fracture. *Nano Lett.* **2017**, *17*, 4568–4575.
[14] Liang, J.; Zhang, J.; Li, Z. Z.; Hong, H.; Wang, J. H.; Zhang, Z. H.; Zhou, X.; Qiao, R. X.; Xu, J. Y.; Gao, P. et al. Monitoring local strain vector in atomic-layered $MoSe_2$ by second-harmonic generation. *Nano Lett.* **2017**, *17*, 7539–7543.
[15] Carrascoso, F.; Li, H.; Frisenda, R.; Castellanos-Gomez, A. Strain engineering in single-, bi- and tri-layer MoS_2, $MoSe_2$, WS_2 and WSe_2. *Nano Res.* **2021**, *14*, 1698–1703.
[16] Carrascoso, F.; Frisenda, R.; Castellanos-Gomez, A. Biaxial versus uniaxial strain tuning of single-layer MoS_2. *Nano Mater. Sci.* **2022**, *4*, 44–51.
[17] Zhang, Q. T.; Yin, J. Spontaneous buckling-driven periodic delamination of thin films on soft substrates under large compression. *J. Mechan. Phys. Solids* **2018**, *118*, 40–57.
[18] Chen, P. Y.; Sodhi, J.; Qiu, Y.; Valentin, T. M.; Steinberg, R. S.; Wang, Z. Y.; Hurt, R. H.; Wong, I. Y. Multiscale graphene topographies programmed by sequential mechanical deformation. *Adv. Mater.* **2016**, *28*, 3564–3571.
[19] Castellanos-Gomez, A.; Roldán, R.; Cappelluti, E.; Buscema, M.; Guinea, F.; Van Der Zant, H. S. J.; Steele, G. A. Local strain engineering in atomically thin MoS_2. *Nano Lett.* **2013**, *13*, 5361–5366.
[20] Ly, T. H.; Yun, S. J.; Thi, Q. H.; Zhao, J. Edge delamination of monolayer transition metal dichalcogenides. *ACS Nano* **2017**, *11*, 7534–7541.
[21] Lou, S.; Liu, Y.; Yang, F. Y.; Lin, S. R.; Zhang, R. P.; Deng, Y.; Wang, M.; Tom, K. B.; Zhou, F.; Ding, H. et al. Three-dimensional architecture enabled by strained two-dimensional material heterojunction. *Nano Lett.* **2018**, *18*, 1819–1825.
[22] Reserbat-Plantey, A.; Kalita, D.; Han, Z.; Ferlazzo, L.; Autier-Laurent, S.; Komatsu, K.; Li, C.; Weil, R.; Ralko, A.; Marty, L. et al. Strain superlattices and macroscale suspension of graphene induced by corrugated substrates. *Nano Lett.* **2014**, *14*, 5044–5051.
[23] Li, H.; Contryman, A. W.; Qian, X. F.; Ardakani, S. M.; Gong, Y. J.; Wang, X. L.; Weisse, J. M.; Lee, C. H.; Zhao, J. H.; Ajayan, P. M. et al. Optoelectronic crystal of artificial atoms in strain-textured molybdenum disulphide. *Nat. Commun.* **2015**, *6*, 7381
[24] Niehues, I.; Schmidt, R.; Drüppel, M.; Marauhn, P.; Christiansen, D.; Selig, M.; Berghäuser, G.; Wigger, D.; Schneider, R.; Braasch, L. et al. Strain control of exciton-phonon coupling in atomically thin semiconductors. *Nano Lett.* **2018**, *18*, 1751–1757
[25] Mohiuddin, T. M. G.; Lombardo, A.; Nair, R. R.; Bonetti, A.; Savini, G.; Jalil, R.; Bonini, N.; Basko, D. M.; Galiotis, C.; Marzari, N. et al. Uniaxial strain in graphene by Raman spectroscopy: *G* peak splitting, Grüneisen parameters, and sample orientation. *Phys. Rev. B* **2009**, *79*, 205433.
[26] He, K. L.; Poole, C.; Mak, K. F.; Shan, J. Experimental demonstration of continuous electronic structure tuning via strain in atomically thin MoS_2. *Nano Lett.* **2013**, *13*, 2931–2936.
[27] Conley, H. J.; Wang, B.; Ziegler, J. I.; Haglund, R. F., Jr.; Pantelides, S. T.; Bolotin, K. I. Bandgap engineering of strained monolayer and bilayer MoS_2. *Nano Lett.* **2013**, *13*, 3626–3630.
[28] Scalise, E.; Houssa, M.; Pourtois, G.; Afanas′ev, V. V.; Stesmans, A. First-principles study of strained 2D MoS_2. *Phys. E: Low-Dimens. Syst. Nanostruct.* **2014**, *56*, 416–421.
[29] Dong, L.; Namburu, R. R.; O'Regan, T. P.; Dubey, M.; Dongare, A. M. Theoretical study on strain-induced variations in electronic properties of monolayer MoS_2. *J. Mater. Sci.* **2014**, *49*, 6762–6771.
[30] Hui, Y. Y.; Liu, X. F.; Jie, W. J.; Chan, N. Y.; Hao, J. H.; Hsu, Y. T.; Li, L. J.; Guo, W. L.; Lau, S. P. Exceptional tunability of band energy in a compressively strained trilayer MoS_2 sheet. *ACS Nano* **2013**, *7*, 7126–7131.
[31] Brennan, C. J.; Nguyen, J.; Yu, E. T.; Lu, N. Interface adhesion between 2D materials and elastomers measured by buckle delaminations. *Adv. Mater. Interfaces.* **2015**, *2*, 1500176.
[32] Li, H.; Sanchez-Santolino, G.; Puebla, S.; Frisenda, R.; Al-Enizi, A. M.; Nafady, A.; D'Agosta, R.; Castellanos-Gomez, A. Strongly anisotropic strain-tunability of excitons in exfoliated $ZrSe_3$. *Adv. Mater.* **2022**, *34*, 2103571.
[33] Li, H.; Lin, D. Y.; Di Renzo, A.; Puebla, S.; Frisenda, R.; Gan, X. T.; Quereda, J.; Xie, Y.; Al-Enizi, A. M.; Nafady, A. et al. Stretching ReS_2 along different crystal directions: Anisotropic tuning of the vibrational and optical responses. *Appl. Phys. Lett.* **2022**, *120*, 063101.
[34] Loginov, Y. N.; Stepanov, S. I.; Golodnov, A. I.; Mukanov, G. Z. Analysis of bending test technique for osteosynthesis titanium plate. *KnE Eng.* **2019**, *1*, 106–112.
[35] Costa, P.; Ferreira, A.; Sencadas, V.; Viana, J. C.; Lanceros-Méndez, S. Electro-mechanical properties of triblock copolymer styrene-butadiene-styrene/carbon nanotube composites for large deformation sensor applications. *Sens. Actuators A Phys.* **2013**, *201*, 458–467.
[36] Castellanos-Gomez, A.; Quereda, J.; Van Der Meulen, H. P.; Agraït, N.; Rubio-Bollinger, G. Spatially resolved optical absorption spectroscopy of single- and few-layer MoS_2 by hyperspectral imaging. *Nanotechnology* **2016**, *27*, 115705.
[37] Niu, Y.; Gonzalez-Abad, S.; Frisenda, R.; Marauhn, P.; Drüppel, M.; Gant, P.; Schmidt, R.; Taghavi, N. S.; Barcons, D.; Molina-Mendoza, A. J. et al. Thickness-dependent differential reflectance spectra of monolayer and few-layer MoS_2, $MoSe_2$, WS_2 and WSe_2. *Nanomaterials* **2018**, *8*, 725.
[38] Chernikov, A.; Berkelbach, T. C.; Hill, H. M.; Rigosi, A.; Li, Y. L.; Aslan, B.; Reichman, D. R.; Hybertsen, M. S.; Heinz, T. F. Exciton binding energy and nonhydrogenic Rydberg series in monolayer WS_2. *Phys. Rev. Lett.* **2014**, *113*, 076802.
[39] Alcaire, M.; Aparicio, F. J.; Obrero, J.; López-Santos, C.; Garcia-Garcia, F. J.; Sánchez-Valencia, J. R.; Frutos, F.; Ostrikov, K.; Borrás, A.; Barranco, A. Plasma enabled conformal and damage free encapsulation of fragile molecular matter: From surface-supported to on-device nanostructures. *Adv. Funct. Mater.* **2019**, *29*, 1903535.
[40] Blake, P.; Hill, E. W.; Neto, A. H.C.; Novoselov, K. S.; Jiang, D.; Yang, R.; Booth, T. J.; Geim, A. K. Making graphene visible. *Appl. Phys. Lett.* **2007**, *91*, 063124.
[41] Li, Z. W.; Lv, Y. W.; Ren, L. W.; Li, J.; Kong, L. G.; Zeng, Y. J.; Tao, Q. Y.; Wu, R. X.; Ma, H. F.; Zhao, B. et al. Efficient strain modulation of 2D materials via polymer encapsulation. *Nat. Commun.* **2020**, *11*, 1151.
[42] Jin, Y.; Ren, Q.; Liu, J.; Zhang, Y.; Zheng, H.; Zhao, P. Stretching graphene to 3.3% strain using formvar-reinforced flexible substrate. *Exp. Mechan.* **2022**, *62*, 761–767.
[43] López-Suárez, M.; Neri, I.; Rurali, R. Band gap engineering of MoS_2 upon compression. *J. Appl. Phys.* **2016**, *119*, 165105
[44] Schmidt, R.; Niehues, I.; Schneider, R.; Drüppel, M.; Deilmann, T.; Rohlfing, M.; De Vasconcellos, S. M.; Castellanos-Gomez, A.; Bratschitsch, R. Reversible uniaxial strain tuning in atomically thin WSe_2. *2D Mater.* **2016**, *3*, 021011.
[45] Xu, C. C.; Zhang, S.; Du, H. Z.; Xue, T.; Kang, Y. L.; Zhang, Y.; Zhao, P.; Li, Q. Y. Revisiting frictional characteristics of graphene: Effect of in-plane straining. *ACS Appl. Mater. Interfaces* **2022**, *14*, 41571–41576.
[46] Frisenda, R.; Niu, Y.; Gant, P.; Molina-Mendoza, A. J.; Schmidt, R.; Bratschitsch, R.; Liu, J. X.; Fu, L.; Dumcenco, D.; Kis, A. et al. Micro-reflectance and transmittance spectroscopy: A versatile and powerful tool to characterize 2D materials. *J. Phys. D Appl. Phys.* **2017**, *50*, 074002.
[47] Frisenda, R.; Navarro-Moratalla, E.; Gant, P.; De Lara, D. P.; Jarillo-Herrero, P.; Gorbachev, R. V.; Castellanos-Gomez, A. Recent progress in the assembly of nanodevices and van der Waals heterostructures by deterministic placement of 2D materials. *Chem. Soc. Rev.* **2018**, *47*, 53–68.
[48] Blaszczyk-Lezak, I.; Aparicio, F. J.; Borrás, A.; Barranco, A.; Álvarez-Herrero, A.; Fernández-Rodríguez, M.; González-Elipe, A. R. Optically active luminescent perylene thin films deposited by plasma polymerization. *J. Phys. Chem. C* **2009**, *113*, 431–438.
[49] Idígoras, J.; Aparicio, F. J.; Contreras-Bernal, L.; Ramos-Terrón, S.; Alcaire, M.; Sánchez-Valencia, J. R.; Borras, A.; Barranco, Á.; Anta, J. A. Enhancing moisture and water resistance in perovskite solar cells by encapsulation with ultrathin plasma polymers. *ACS Appl. Mater. Interfaces* **2018**, *10*, 11587–11594.